

Femtoscopy can tell whether $Z_c(3900)$ and $Z_{cs}(3985)$ are resonances, virtual states, or bound states

Zhi-Wei Liu,¹ Jun-Xu Lu,^{1,*} Ming-Zhu Liu,^{2,3} and Li-Sheng Geng^{1,4,5,6,7,†}

¹School of Physics, Beihang University, Beijing 102206, China

²Frontiers Science Center for Rare Isotopes, Lanzhou University, Lanzhou 730000, China

³School of Nuclear Science and Technology, Lanzhou University, Lanzhou 730000, China

⁴Centrale Pékin, Beihang University, Beijing, 100191, China

⁵Peng Huanwu Collaborative Center for Research and Education, Beihang University, Beijing 100191, China

⁶Beijing Key Laboratory of Advanced Nuclear Materials and Physics, Beihang University, Beijing 102206, China

⁷Southern Center for Nuclear-Science Theory (SCNT), Institute of Modern Physics, Chinese Academy of Sciences, Huizhou 516000, China

There have been extended and heated discussions on the nature of the two exotic states, $Z_c(3900)$ and $Z_{cs}(3985)$, particularly whether they are near-threshold resonances, virtual states or bound states. In this work, we demonstrate for the first time that the femtoscopic technique can be used to unambiguously distinguish between these three scenarios. More concretely, we show that the low-momentum $D^0 D^{*-}/D^0 D_s^{*-}$ correlation functions significantly differ in the three scenarios. The high-momentum results exhibit distinct characteristics in the resonant and virtual state scenarios, especially in small collision systems of 1 fm, as produced in pp collisions at the LHC. We hope all these discoveries can stimulate further experimental studies and help clarify the nature of the many exotic states discovered.

Introduction.—In 2013, the BESIII Collaboration and Belle Collaboration observed a hidden-charm tetraquark candidate $Z_c(3900)^{\pm}$ in the $J/\psi\pi^{\pm}$ invariant mass distribution of the $e^+e^- \rightarrow J/\psi\pi^+\pi^-$ process [1, 2]. This charged charmoniumlike state was subsequently confirmed by the CLEO-c Collaboration in the e^+e^- annihilation process [3] and the semi-inclusive decays of b -hadrons at the D0 experiment [4]. In 2020, the BESIII Collaboration reported the first signal of a hidden-charm state with strangeness, $Z_{cs}(3985)^-$, in the K^+ recoil-mass spectrum of the $e^+e^- \rightarrow K^+(D^{*0}D_s^- + D^0D_s^{*-})$ reaction [5]. Since the quark contents of the charged $Z_c(3900)^-/Z_c(3900)^+$ and $Z_{cs}(3985)^-$ states are $c\bar{c}d\bar{u}/c\bar{c}u\bar{d}$ and $c\bar{c}s\bar{u}$, respectively, the latter is often interpreted as the strangeness partner of the former in terms of the SU(3)-flavor symmetry. We note that their isospin quantum numbers have been fixed by the discovery of their neutral partners [6, 7].

There have been extensive studies on the nature of the $Z_c(3900)/Z_{cs}(3985)$ states, treating them as hadronic molecules of $D^0 D^{*-}/D^0 D_s^{*-}$ [8–20], compact tetraquark states [21–23], or threshold effects [24–27](see Refs. [28–34] for recent reviews), but no firm conclusion has been reached. Especially due to the lack of reliable theoretical understanding of the $D^0 D^{*-}$ and $D^0 D_s^{*-}$ interactions, there have been long and heated discussions on whether $Z_c(3900)$ and $Z_{cs}(3985)$ are resonances, virtual states, or bound states. In the experimental analyses based on the Breit-Wigner parametrization, $Z_c(3900)$ and $Z_{cs}(3985)$ are suggested to be typical resonances [1, 2, 5]. However, various theoretical re-analyses of the same data suggest they can be either resonances, virtual states, or bound states [9–20]. The lattice QCD simulations of coupled-channel $\pi J/\psi$, $\rho\eta_c$, and $\bar{D}D^*$ interactions at $m_\pi = 400 - 710$ MeV even indicates that the $Z_c(3900)$ is a threshold cusp [35], which can produce the lineshapes of $Y(4260)$ consistent with the BESIII data [1, 36].

In recent years, femtoscopy, which measures two-hadron momentum correlation functions (CFs), has made remarkable progress in revealing the dynamics of the strong interactions between pairs of stable and unstable hadrons [37–39]. Thanks to the abundant rare hadrons produced and the various particle emission sources available in relativistic pp , pA , and AA collisions, the femtoscopic technique can be used not only to study the strong interactions involving unstable hadrons that are difficult or impossible in traditional scattering experiments but also to provide more and complementary information compared with the measurement of invariant mass distributions. A lot has been learned about the meson-meson [40–44], meson-baryon [45–49], and (anti)baryon-(anti)baryon [50–62] interactions in the light quark (u, d, s) sector with the femtoscopic technique. More recently, the successful measurements of the $\bar{D}N$, $D^{(*)}\pi$, and $D^{(*)}K$ CFs demonstrated the huge potential to access the charm sector experimentally [63, 64]. With the upgraded ALICE apparatus and the larger data sample expected at LHC runs 3, 4, and 5, more reactions can be accessed with high precision in the future [65].

On the other hand, the experimental studies have also triggered a large number of theoretical studies [66–78], especially in the charm and bottom sectors [79–91]. It was shown that femtoscopy offers a valuable means to directly test the hadronic molecular picture of the exotic hadrons [81–84]. However, it is worth noting that the above studies mainly focus on bound states, with little discussion about resonant or virtual states. In this letter, we show how one can utilize the femtoscopic technique to study hadronic interaction in the presence of near-threshold resonances, virtual states, or bound states. In particular, assuming that $Z_c(3900)/Z_{cs}(3985)$ is a molecular state of $D^0 D^{*-}/D^0 D_s^{*-}$, one can distinguish whether $Z_c(3900)/Z_{cs}(3985)$ is a resonance, a virtual state, or a bound state by measuring the $D^0 D^{*-}/D^0 D_s^{*-}$ CFs.

Model-independent formulations of the $D^0 D^{-}/D^0 D_s^{*-}$ interactions and corresponding correlation functions.*—Close to the threshold, the most general S -wave potential up to the next-to-leading order in momentum expansion has the follow-

* Corresponding author: ljxwohol@buaa.edu.cn

† Corresponding author: lisheng.geng@buaa.edu.cn

ing form

$$V(k) = a + b k^2, \quad (1)$$

where $k = \frac{\sqrt{s-(m_1+m_2)^2}\sqrt{s-(m_1-m_2)^2}}{2\sqrt{s}}$ represents the center-of-mass (c.m.) momentum of the particle pair with masses $m_{1,2}$, and a and b are (real) low-energy constants (LECs) to be determined. Then, the single-channel T -matrix can be obtained as

$$T(\sqrt{s}) = (1 - VG)^{-1} V = -\rho^{-1} e^{i\delta} \sin \delta, \quad (2)$$

where \sqrt{s} represents the c.m. energy, δ is the phase shift, and $\rho = k/(8\pi\sqrt{s})$ is the phase-space factor. The loop function (in the first/physical Riemann sheet (RS)) G is regularized by a sharp cutoff q_{\max} of the order of $0.8 - 1.2$ GeV,

$$G(\sqrt{s}) = \int_0^{q_{\max}} \frac{d^3k'}{(2\pi)^3} \frac{E'_1 + E'_2}{2E'_1 E'_2} \frac{1}{s - (E'_1 + E'_2)^2 + i\varepsilon}, \quad (3)$$

with $E_i = \sqrt{m_i^2 + k'^2}$. Here, virtual (bound) and resonant states are identified as poles in the second (first) RS of the T -matrix on the real axis below the threshold and the complex \sqrt{s} plane, respectively. For a resonance, the real and imaginary parts of the pole position define its mass and half-width. The loop function in the second/unphysical RS, G^{II} , is related to that in the first RS by an analytic continuation as $G^{\text{II}} = G + 2i\rho$ [92]. In addition, it is worth calculating the scattering length a_0 and effective range r_{eff} [84]

$$-\frac{1}{a_0} = [-8\pi\sqrt{s}T^{-1}]_{m_1+m_2}, \quad (4a)$$

$$r_{\text{eff}} = \left[\frac{\partial^2}{\partial k^2} (-8\pi\sqrt{s}T^{-1} + ik) \right]_{m_1+m_2}. \quad (4b)$$

According to the Koonin-Pratt formula [93–95], the femtoscopic CF depends on two quantities, namely, ψ the scattering wave function of the relative motion for the pair of interest and S_{12} the particle-emitting source created in relativistic pp , pA , and AA collisions. The former contains the information on the final-state interaction we are interested in. In general, there are two ways to obtain the scattering wave function, either by solving the Schrödinger equation in coordinate space [96, 97] or the Lippmann-Schwinger (Bethe-Salpeter) equation in momentum space [81, 98]. In this work, since the potential of Eq. (1) is constructed in momentum space, it is convenient first to obtain the reaction amplitude T -matrix by solving Eq. (2) and then derive the scattering wave function using the relation $|\psi\rangle = |\varphi\rangle + GT|\varphi\rangle$, where G and $|\varphi\rangle$ represent the free propagator and wave function. For the particle-emitting source, a data-driven approach named the resonance source model proposed by the ALICE Collaboration has been widely employed in the femtoscopic analyses [47, 56, 59–61, 63], based on the hypothesis of a common emission source for all hadrons in small collision systems. In this model, the source is characterized by a Gaussian core that emits all primordial particles, complemented

by an exponential tail arising from strongly decaying resonances [99, 100]. The core size R shows a clear transverse mass (m_T) scaling [99, 100], which is commonly associated with collective effects (such as radial flow as previously observed in heavy-ion collisions) and has been reproduced successfully in the single-particle emission model CECA by introducing spacial-momentum correlations [101]. The resonance yields and decay kinematics are estimated using the thermal and transport models [102, 103]. In the present work, given the expected minimal contribution from the strong decays feeding into charm mesons [63], it is pertinent to adopt a Gaussian source $S_{12} = \exp[-r^2/(4R^2)]/(2\sqrt{\pi}R)^3$ in this exploratory study. The source size R can be anchored to the proton-proton correlation data by measuring m_T of the pair of interest in future experiments. With the above-specified ingredients, the CF is expressed as [83]

$$C(k) = 1 + \int_0^\infty d^3r S_{12} \left[|j_0 + T\tilde{G}|^2 - |j_0|^2 \right], \quad (5a)$$

$$= 1 + \mathcal{F}_1 \sin^2 \delta + \mathcal{F}_2 \sin \delta \cos \delta, \quad (5b)$$

where $j_0(kr)$ is the spherical Bessel function, $\mathcal{F}_1 = \int d^3r S_{12} [(\text{Re}\tilde{G}/\rho)^2 - |j_0|^2]$, and $\mathcal{F}_2 = -\int d^3r S_{12} 2j_0 \text{Re}\tilde{G}/\rho$. The quantity \tilde{G} is given by

$$\tilde{G}(r, \sqrt{s}) = \int_0^{q_{\max}} \frac{d^3k'}{(2\pi)^3} \frac{E'_1 + E'_2}{2E'_1 E'_2} \frac{j_0(k'r)}{s - (E'_1 + E'_2)^2 + i\varepsilon}. \quad (6)$$

It is worthwhile to emphasize that Eq. (5b) establishes a clear relationship between the femtoscopic CF and the scattering phase shift, which is difficult or impossible to obtain through scattering experiments for unstable hadrons.

As mentioned above, a , b , and q_{\max} are the only unknown parameters in describing the $D^0 D^{*-}/D^0 D_s^{*-}$ interaction. They can be determined by reproducing the pole positions of $Z_c(3900)/Z_{cs}(3985)$ in the three scenarios of resonant/virtual/bound state. We adopt the latest PDG averages for the resonant state poles [104] and fine-tune the virtual/bound state pole to obtain a line shape for the $D^0 D^{*-}/D^0 D_s^{*-}$ invariant mass spectrum (IMS) similar to that of the resonant state scenario. These pole settings, LECs a , b , the scattering length, and the effective range are listed in Table I. The adopted virtual state poles of $Z_c(3900)$ and $Z_{cs}(3985)$ are compatible with the theoretical results [9–11, 13, 16–18, 20], and the adopted bound state poles of $Z_c(3900)$ and $Z_{cs}(3985)$ are close to the results of Ref. [16]. In addition, it has been demonstrated that virtual and bound states generated by a constant potential are dominantly hadronic molecules [12], but introducing an additional momentum-dependent term can lead to the emergence of non-molecular components. The large negative effective range, as listed in Table I, suggests that the non-molecular component may play a relevant role in the resonant state scenario of $Z_c(3900)/Z_{cs}(3985)$.

Results and discussions.—Before studying CFs, it is necessary to discuss the properties of $|T|^2$, $\rho|T|^2$, and δ for the three scenarios, as shown in Fig. 1. Since the virtual and bound

TABLE I. Masses and widths of $Z_c(3900)$ and $Z_{cs}(3985)$, the LECs a , b , the scattering length a_0 , and the effective range r_{eff} . The $D^0 D^{*-}$ and $D^0 D_s^{*-}$ thresholds are 3875.1 MeV and 3977.04 MeV, respectively. The uncertainties for a , b , a_0 , and r_{eff} originate from the variation of the sharp cutoff q_{max} in the range of $q_{\text{max}} = 0.8 - 1.2$ GeV.

Scenario	M [MeV]	Γ [MeV]	a	b [10 $^{-6}$ MeV $^{-2}$]	a_0 [fm]	r_{eff} [fm]
$Z_c(3900)$	resonant	3887.1 [104]	28.4 [104]	-101.7 ± 8.3	-1380.6 ± 617.8	-0.6 ± 0.1
	virtual	3871	0	-137.9 ± 26.6	0	-2.1 ± 0.0
	bound	3867	0	-196.0 ± 57.8	0	1.7 ± 0.0
$Z_{cs}(3985)$	resonant	3988 [104]	14 [104]	-87.9 ± 3.9	-2686.7 ± 1284.4	-0.4 ± 0.1
	virtual	3974	0	-144.0 ± 28.6	0	-2.4 ± 0.0
	bound	3972	0	-192.5 ± 54.4	0	2.1 ± 0.0

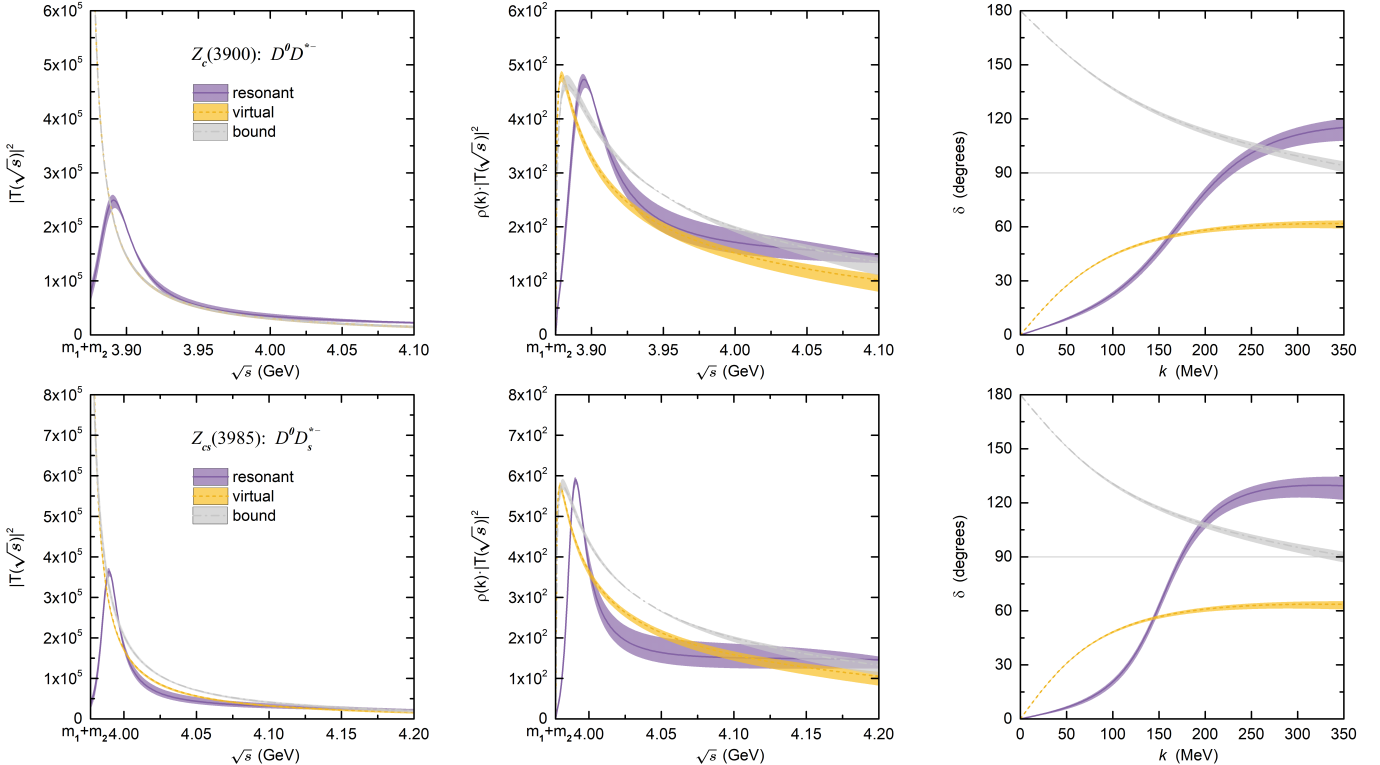


FIG. 1. $D^0 D^{*-}$ (upper) and $D^0 D_s^{*-}$ (lower) $|T|^2$, $\rho|T|^2$ as a function of the c.m. energy \sqrt{s} , and the phase shifts as a function of the relative momentum k . The bands reflect the variation of the sharp cutoff in the range of $q_{\text{max}} = 0.8 - 1.2$ GeV.

state poles lie on the real axis below the threshold, while the resonant state pole lies above the threshold and deviates from the real axis, $|T|^2$ for virtual and bound states near the threshold $m_1 + m_2$ are significantly larger than those for resonant states. However, $|T|^2$ is not directly observable; the measurable IMS is proportional to $\rho|T|^2$ [105]. Due to the phase-space suppression near the threshold, IMSs of virtual and bound states exhibit resonance-like shapes, as $\rho|T|^2$ depicts. This explains why it is difficult to distinguish near-threshold resonant/virtual/bound states through IMSs with limited experimental resolution. On the other hand, δ exhibits unique features in the three scenarios. For instance, the resonant and virtual states δ start from 0° and increase with momentum/energy; the bound state δ starts at 180° and decreases; as momentum increases, the resonant state δ exceeds 90° around

the resonant energy.

We present the $D^0 D^{*-}$ (upper) and $D^0 D_s^{*-}$ CFs (lower) for three typical source sizes $R = 1, 2$, and 5 fm in Fig. 2, where the left/middle/right panel corresponds to the results in the resonant/virtual/bound state scenarios. In the resonant state scenario, the $D^0 D^{*-}$ CF is enhanced (compared to unity) in the low-momentum region but suppressed in the high-momentum region and exhibits a minimum. This resonance behavior can be understood from Eq. (5b): as the momentum increases and δ crosses 90° , $\mathcal{F}_2 \sin \delta \cos \delta$ changes from positive to negative because \mathcal{F}_2 is always positive in the present work. In the virtual state scenario, the $D^0 D^{*-}$ CF shows an enhancement in a wide range of k , with a particularly strong enhancement in the low-momentum region, which can be traced to the increasing virtual state $|T|^2$ near

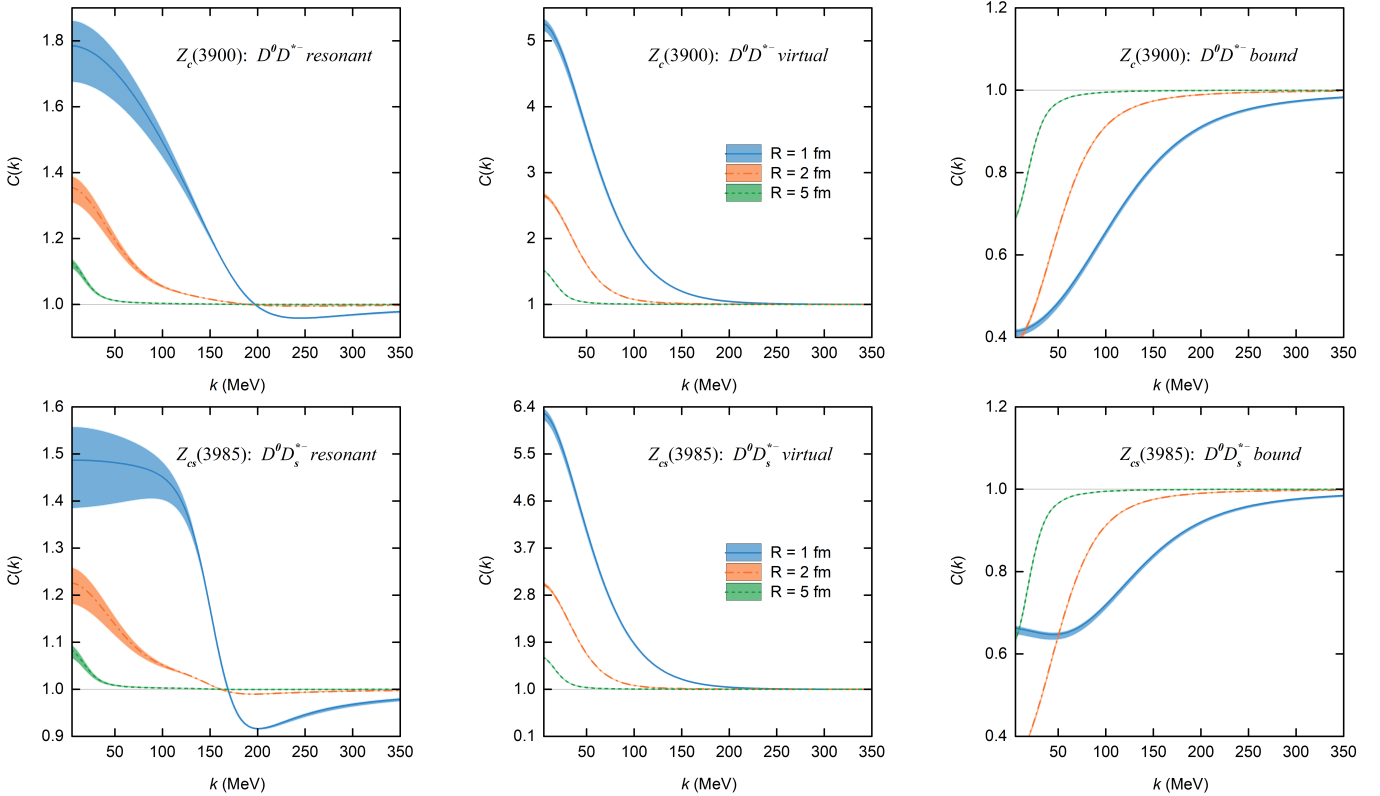


FIG. 2. $D^0 D^{*-}$ (upper) and $D^0 D_s^{*-}$ (lower) correlation functions as a function of the relative momentum k for different source sizes $R = 1$, 2, and 5 fm. The bands reflect the variation of the sharp cutoff in the range of $q_{\max} = 0.8 - 1.2$ GeV.

the threshold. In the bound state scenario, the $D^0 D^{*-}$ CF is suppressed in a wide range of k , which is similar to the result obtained with a strongly attractive potential in the square-well model [81] (this point can also be obtained by analyzing the bound state δ). As the source size R decreases, the difference in the CFs between these three scenarios becomes more significant because of the short-range nature of the strong interaction.

Due to the SU(3)-flavor symmetry, the $D^0 D_s^{*-}$ CFs exhibit similar behaviors as the $D^0 D^{*-}$ CFs. However, in the resonant state scenario, the suppression in the high-momentum region becomes more pronounced, which can be attributed to the narrower width of $Z_{cs}(3985)$. This is understandable because as the pole approaches the real axis, the influence of the resonant structure on physical observables intensifies. We emphasize that experimentally it is feasible to distinguish whether $Z_c(3900)/Z_{cs}(3985)$ is a resonant/virtual/bound state by measuring the $D^0 D^{*-}/D^0 D_s^{*-}$ CFs, especially in pp collisions. This is because, on the one hand, the three CFs differ significantly in numerical values and exhibit distinct characteristics in the low-momentum region. On the other hand, the experimental uncertainties in the high-momentum region are usually much smaller than those in the low-momentum region (see, e.g., Refs [40–64]). Our results show that for the $D^0 D^{*-}$ and $D^0 D_s^{*-}$ CFs, the relative difference in the CFs between the resonant and virtual scenarios can be as significant as about 7% and 17% for $R = 1$ fm, and even about

10% and 23% for $R = 0.9$ fm at $k \approx 230$ and $k \approx 180$ MeV, respectively.

Before closing our discussion, some comments are relevant in understanding the robustness of the results: i) Coupled-channel effects [69, 91]. For the $D^0 D^{*-}$ CF, the $\pi J/\psi - D\bar{D}^*$ coupled-channel effect may offset the high-momentum suppression in the resonant state scenario. However, the significant differences in the low-momentum region can still distinguish the three scenarios. For the $D^0 D_s^{*-}$ CF, the $\bar{K}J/\psi - D\bar{D}_s^*$ coupled-channel effect can be safely neglected due to the small inelastic transition between $D\bar{D}_s^*$ and $\bar{K}J/\psi$ [106]. ii) Effect of the uncertainty of pole positions. We have checked that even accounting for the uncertainties of pole positions (e.g., $Z_{cs}(3985)$ resonant pole $3988_{-5}^{+5} + i14_{-4}^{+4}$ MeV [104], virtual pole $3974_{-1.0}^{+1.3}$ MeV, and bound pole $3972_{-2.2}^{+2.5}$ MeV), CFs can still distinguish whether $Z_c(3900)$ and $Z_{cs}(3985)$ are resonant, virtual, or bound states. In addition, stricter constraints, especially for the shallow bound state, can be obtained by measuring the CFs in pp , pA , and AA collisions. iii) Comparison with the Lednický-Lyuboshits (LL) model [37, 38, 107]. With the scattering parameters listed in Table I, the LL model can reproduce the CFs for virtual and bound state scenarios. However, for resonant state scenarios where $|r_{\text{eff}}|$ is much larger than the source size R , the effective range correction may introduce significant deviations. Therefore, we suggest using Eq. (5b) proposed in this work to extract phase shifts from experimen-

tal CFs in future studies. (see the Supplemental Material for more details)

Summary and outlook.—In this letter, we proposed to decipher the nature of $Z_c(3900)$ and $Z_{cs}(3985)$ with the femtoscopic technique. We first evaluated the $D^0 D^{*-}/D^0 D_s^{*-}$ interactions by reproducing the pole positions of $Z_c(3900)/Z_{cs}(3985)$ in the resonance, virtual state, and bound state scenarios, respectively. We noted that the phase-space suppression effect is the main reason for the difficulty in distinguishing the near-threshold states using the invariant mass spectrum alone. We found that the low-momentum $D^0 D^{*-}/D^0 D_s^{*-}$ correlation functions are significantly different in the three scenarios. The high-momentum results exhibit distinct characteristics in the resonant and virtual state scenarios, especially in small collision systems of the order of 1 fm, as produced in pp collisions at the LHC. The novel approach is powerful enough to distinguish whether $Z_c(3900)$ and $Z_{cs}(3985)$ are resonances, virtual states, or bound states unambiguously. In addition, we established a clear relationship between the femtoscopic correlation function and the scattering phase shifts, which can help extract the strong interactions between hadron pairs from correlation

functions.

Considering the experimental precision achievable at present and future facilities, we strongly encourage measuring the $D^0 D^{*-}/D^0 D_s^{*-}$ correlation functions in pp , pA , and AA collisions. It is important to note that the proposed method is model-independent. This results from the general features of femtoscopic correlation functions and the effective field theory description of the strong interactions close to the threshold. It can be applied to clarify the nature of other similar exotic states, such as $Z_c(4020)$, $Z_b(10610)$, and $Z_b(10650)$.

Acknowledgments. We thank Eulogio Oset for a careful reading of the original manuscript. We also thank the anonymous referees for their valuable comments, which helped greatly improve our manuscript. This work is partly supported by the National Key R&D Program of China under Grant No. 2023YFA1606700 and the National Natural Science Foundation of China under Grant No. 12435007. Zhi-Wei Liu acknowledges support from the National Natural Science Foundation of China under Grant No.12405133, No.12347180, China Postdoctoral Science Foundation under Grant No.2023M740189, and the Postdoctoral Fellowship Program of CPSF under Grant No.GZC20233381.

-
- [1] M. Ablikim *et al.* (BESIII), *Phys. Rev. Lett.* **110**, 252001 (2013), arXiv:1303.5949 [hep-ex].
 - [2] Z. Q. Liu *et al.* (Belle), *Phys. Rev. Lett.* **110**, 252002 (2013), [Erratum: *Phys. Rev. Lett.* **111**, 019901 (2013)], arXiv:1304.0121 [hep-ex].
 - [3] T. Xiao, S. Dobbs, A. Tomaradze, and K. K. Seth, *Phys. Lett. B* **727**, 366 (2013), arXiv:1304.3036 [hep-ex].
 - [4] V. M. Abazov *et al.* (D0), *Phys. Rev. D* **98**, 052010 (2018), arXiv:1807.00183 [hep-ex].
 - [5] M. Ablikim *et al.* (BESIII), *Phys. Rev. Lett.* **126**, 102001 (2021), arXiv:2011.07855 [hep-ex].
 - [6] M. Ablikim *et al.* (BESIII), *Phys. Rev. Lett.* **115**, 112003 (2015), arXiv:1506.06018 [hep-ex].
 - [7] M. Ablikim *et al.* (BESIII), *Phys. Rev. Lett.* **129**, 112003 (2022), arXiv:2204.13703 [hep-ex].
 - [8] Q. Wang, C. Hanhart, and Q. Zhao, *Phys. Rev. Lett.* **111**, 132003 (2013), arXiv:1303.6355 [hep-ph].
 - [9] F.-K. Guo, C. Hidalgo-Duque, J. Nieves, and M. P. Valderrama, *Phys. Rev. D* **88**, 054007 (2013), arXiv:1303.6608 [hep-ph].
 - [10] M. Albaladejo, F.-K. Guo, C. Hidalgo-Duque, and J. Nieves, *Phys. Lett. B* **755**, 337 (2016), arXiv:1512.03638 [hep-ph].
 - [11] J. He and D.-Y. Chen, *Eur. Phys. J. C* **78**, 94 (2018), arXiv:1712.05653 [hep-ph].
 - [12] F.-K. Guo, C. Hanhart, U.-G. Meißner, Q. Wang, Q. Zhao, and B.-S. Zou, *Rev. Mod. Phys.* **90**, 015004 (2018), [Erratum: *Rev. Mod. Phys.* **94**, 029901 (2022)], arXiv:1705.00141 [hep-ph].
 - [13] Z. Yang, X. Cao, F.-K. Guo, J. Nieves, and M. P. Valderrama, *Phys. Rev. D* **103**, 074029 (2021), arXiv:2011.08725 [hep-ph].
 - [14] M.-J. Yan, F.-Z. Peng, M. Sánchez Sánchez, and M. Pavon Valderrama, *Phys. Rev. D* **104**, 114025 (2021), arXiv:2102.13058 [hep-ph].
 - [15] L. Meng, B. Wang, and S.-L. Zhu, *Phys. Rev. D* **102**, 111502 (2020), arXiv:2011.08656 [hep-ph].
 - [16] V. Baru, E. Epelbaum, A. A. Filin, C. Hanhart, and A. V. Nefediev, *Phys. Rev. D* **105**, 034014 (2022), arXiv:2110.00398 [hep-ph].
 - [17] M.-L. Du, M. Albaladejo, F.-K. Guo, and J. Nieves, *Phys. Rev. D* **105**, 074018 (2022), arXiv:2201.08253 [hep-ph].
 - [18] T. Ji, X.-K. Dong, M. Albaladejo, M.-L. Du, F.-K. Guo, and J. Nieves, *Phys. Rev. D* **106**, 094002 (2022), arXiv:2207.08563 [hep-ph].
 - [19] L.-W. Yan, Z.-H. Guo, F.-K. Guo, D.-L. Yao, and Z.-Y. Zhou, *Phys. Rev. D* **109**, 014026 (2024), arXiv:2307.12283 [hep-ph].
 - [20] Y.-H. Chen, M.-L. Du, and F.-K. Guo, *Sci. China Phys. Mech. Astron.* **67**, 291011 (2024), arXiv:2310.15965 [hep-ph].
 - [21] Z.-G. Wang, *Chin. Phys. C* **45**, 073107 (2021), arXiv:2011.10959 [hep-ph].
 - [22] L. Maiani, A. D. Polosa, and V. Riquer, *Sci. Bull.* **66**, 1616 (2021), arXiv:2103.08331 [hep-ph].
 - [23] R.-H. Wu, C.-Y. Wang, C. Meng, Y.-Q. Ma, and K.-T. Chao, *JHEP* **06**, 216 (2024), arXiv:2312.14224 [hep-ph].
 - [24] D.-Y. Chen, X. Liu, and T. Matsuki, *Phys. Rev. D* **88**, 036008 (2013), arXiv:1304.5845 [hep-ph].
 - [25] J.-Z. Wang, Q.-S. Zhou, X. Liu, and T. Matsuki, *Eur. Phys. J. C* **81**, 51 (2021), arXiv:2011.08628 [hep-ph].
 - [26] N. Ikeno, R. Molina, and E. Oset, *Phys. Lett. B* **814**, 136120 (2021), arXiv:2011.13425 [hep-ph].
 - [27] S. Prelovsek, C. B. Lang, L. Leskovec, and D. Mohler, *Phys. Rev. D* **91**, 014504 (2015), arXiv:1405.7623 [hep-lat].
 - [28] S. L. Olsen, T. Skwarnicki, and D. Zieminska, *Rev. Mod. Phys.* **90**, 015003 (2018), arXiv:1708.04012 [hep-ph].
 - [29] M. Karliner, J. L. Rosner, and T. Skwarnicki, *Ann. Rev. Nucl. Part. Sci.* **68**, 17 (2018), arXiv:1711.10626 [hep-ph].
 - [30] C.-Z. Yuan, *Int. J. Mod. Phys. A* **33**, 1830018 (2018), arXiv:1808.01570 [hep-ex].
 - [31] Y.-R. Liu, H.-X. Chen, W. Chen, X. Liu, and S.-L. Zhu, *Prog. Part. Nucl. Phys.* **107**, 237 (2019), arXiv:1903.11976 [hep-ph].
 - [32] N. Brambilla, S. Eidelman, C. Hanhart, A. Nefediev, C.-P.

- Shen, C. E. Thomas, A. Vairo, and C.-Z. Yuan, *Phys. Rept.* **873**, 1 (2020), arXiv:1907.07583 [hep-ex].
- [33] F.-K. Guo, X.-H. Liu, and S. Sakai, *Prog. Part. Nucl. Phys.* **112**, 103757 (2020), arXiv:1912.07030 [hep-ph].
- [34] L. Meng, B. Wang, G.-J. Wang, and S.-L. Zhu, *Phys. Rept.* **1019**, 1 (2023), arXiv:2204.08716 [hep-ph].
- [35] Y. Ikeda, S. Aoki, T. Doi, S. Gongyo, T. Hatsuda, T. Inoue, T. Iritani, N. Ishii, K. Murano, and K. Sasaki (HAL QCD), *Phys. Rev. Lett.* **117**, 242001 (2016), arXiv:1602.03465 [hep-lat].
- [36] M. Ablikim *et al.* (BESIII), *Phys. Rev. Lett.* **112**, 022001 (2014), arXiv:1310.1163 [hep-ex].
- [37] S. Cho *et al.* (ExHIC), *Prog. Part. Nucl. Phys.* **95**, 279 (2017), arXiv:1702.00486 [nucl-th].
- [38] L. Fabbietti, V. Mantovani Sarti, and O. Vazquez Doce, *Ann. Rev. Nucl. Part. Sci.* **71**, 377 (2021), arXiv:2012.09806 [nucl-ex].
- [39] M.-Z. Liu, Y.-W. Pan, Z.-W. Liu, T.-W. Wu, J.-X. Lu, and L.-S. Geng, *Phys. Rept.* **1108**, 1 (2025), arXiv:2404.06399 [hep-ph].
- [40] S. Acharya *et al.* (ALICE), *Phys. Lett. B* **774**, 64 (2017), arXiv:1705.04929 [nucl-ex].
- [41] S. Acharya *et al.* (ALICE), *Phys. Lett. B* **790**, 22 (2019), arXiv:1809.07899 [nucl-ex].
- [42] S. Acharya *et al.* (ALICE), *Phys. Lett. B* **813**, 136030 (2021), arXiv:2007.08315 [nucl-ex].
- [43] S. Acharya *et al.* (ALICE), *Phys. Lett. B* **833**, 137335 (2022), arXiv:2111.06611 [nucl-ex].
- [44] S. Acharya *et al.* (ALICE), *Phys. Lett. B* **856**, 138915 (2024), arXiv:2312.12830 [hep-ex].
- [45] S. Acharya *et al.* (ALICE), *Phys. Rev. Lett.* **124**, 092301 (2020), arXiv:1905.13470 [nucl-ex].
- [46] S. Acharya *et al.* (ALICE), *Phys. Rev. C* **103**, 055201 (2021), arXiv:2005.11124 [nucl-ex].
- [47] S. Acharya *et al.* (ALICE), *Phys. Rev. Lett.* **127**, 172301 (2021), arXiv:2105.05578 [nucl-ex].
- [48] S. Acharya *et al.* (ALICE), *Eur. Phys. J. C* **83**, 340 (2023), arXiv:2205.15176 [nucl-ex].
- [49] S. Acharya *et al.* (ALICE), *Phys. Lett. B* **845**, 138145 (2023), arXiv:2305.19093 [nucl-ex].
- [50] L. Adamczyk *et al.* (STAR), *Phys. Rev. Lett.* **114**, 022301 (2015), arXiv:1408.4360 [nucl-ex].
- [51] L. Adamczyk *et al.* (STAR), *Nature* **527**, 345 (2015), arXiv:1507.07158 [nucl-ex].
- [52] J. Adam *et al.* (STAR), *Phys. Lett. B* **790**, 490 (2019), arXiv:1808.02511 [hep-ex].
- [53] M. Isshiki (STAR), *EPJ Web Conf.* **259**, 11015 (2022), arXiv:2109.10953 [nucl-ex].
- [54] S. Acharya *et al.* (ALICE), *Phys. Rev. C* **99**, 024001 (2019), arXiv:1805.12455 [nucl-ex].
- [55] S. Acharya *et al.* (ALICE), *Phys. Lett. B* **797**, 134822 (2019), arXiv:1905.07209 [nucl-ex].
- [56] S. Acharya *et al.* (ALICE), *Phys. Lett. B* **805**, 135419 (2020), arXiv:1910.14407 [nucl-ex].
- [57] S. Acharya *et al.* (ALICE), *Phys. Lett. B* **802**, 135223 (2020), arXiv:1903.06149 [nucl-ex].
- [58] S. Acharya *et al.* (ALICE), *Phys. Rev. Lett.* **123**, 112002 (2019), arXiv:1904.12198 [nucl-ex].
- [59] A. Collaboration *et al.* (ALICE), *Nature* **588**, 232 (2020), [Erratum: Nature 590, E13 (2021)], arXiv:2005.11495 [nucl-ex].
- [60] S. Acharya *et al.* (ALICE), *Phys. Lett. B* **833**, 137272 (2022), arXiv:2104.04427 [nucl-ex].
- [61] S. Acharya *et al.* (ALICE), *Phys. Lett. B* **829**, 137060 (2022), arXiv:2105.05190 [nucl-ex].
- [62] S. Acharya *et al.* (ALICE), *Phys. Lett. B* **844**, 137223 (2023), arXiv:2204.10258 [nucl-ex].
- [63] S. Acharya *et al.* (ALICE), *Phys. Rev. D* **106**, 052010 (2022), arXiv:2201.05352 [nucl-ex].
- [64] S. Acharya *et al.* (ALICE), *Phys. Rev. D* **110**, 032004 (2024), arXiv:2401.13541 [nucl-ex].
- [65] (2022), arXiv:2211.02491 [physics.ins-det].
- [66] K. Morita, T. Furumoto, and A. Ohnishi, *Phys. Rev. C* **91**, 024916 (2015), arXiv:1408.6682 [nucl-th].
- [67] K. Morita, A. Ohnishi, F. Etminan, and T. Hatsuda, *Phys. Rev. C* **94**, 031901 (2016), [Erratum: Phys.Rev.C 100, 069902 (2019)], arXiv:1605.06765 [hep-ph].
- [68] A. Ohnishi, K. Morita, K. Miyahara, and T. Hyodo, *Nucl. Phys. A* **954**, 294 (2016), arXiv:1603.05761 [nucl-th].
- [69] J. Haidenbauer, *Nucl. Phys. A* **981**, 1 (2019), arXiv:1808.05049 [hep-ph].
- [70] K. Morita, S. Gongyo, T. Hatsuda, T. Hyodo, Y. Kamiya, and A. Ohnishi, *Phys. Rev. C* **101**, 015201 (2020), arXiv:1908.05414 [nucl-th].
- [71] Y. Kamiya, T. Hyodo, K. Morita, A. Ohnishi, and W. Weise, *Phys. Rev. Lett.* **124**, 132501 (2020), arXiv:1911.01041 [nucl-th].
- [72] K. Ogata, T. Fukui, Y. Kamiya, and A. Ohnishi, *Phys. Rev. C* **103**, 065205 (2021), arXiv:2103.00100 [nucl-th].
- [73] Y. Kamiya, K. Sasaki, T. Fukui, T. Hyodo, K. Morita, K. Ogata, A. Ohnishi, and T. Hatsuda, *Phys. Rev. C* **105**, 014915 (2022), arXiv:2108.09644 [hep-ph].
- [74] J. Haidenbauer and U.-G. Meißner, *Phys. Lett. B* **829**, 137074 (2022), arXiv:2109.11794 [nucl-th].
- [75] Z.-W. Liu, K.-W. Li, and L.-S. Geng, *Chin. Phys. C* **47**, 024108 (2023), arXiv:2201.04997 [hep-ph].
- [76] R. Molina, C.-W. Xiao, W.-H. Liang, and E. Oset, *Phys. Rev. D* **109**, 054002 (2024), arXiv:2310.12593 [hep-ph].
- [77] R. Molina, Z.-W. Liu, L.-S. Geng, and E. Oset, *Eur. Phys. J. C* **84**, 328 (2024), arXiv:2312.11993 [hep-ph].
- [78] V. M. Sarti, A. Feijoo, I. Vidaña, A. Ramos, F. Giacosa, T. Hyodo, and Y. Kamiya, *Phys. Rev. D* **110**, L011505 (2024), arXiv:2309.08756 [hep-ph].
- [79] J. Haidenbauer, G. Krein, and T. C. Peixoto, *Eur. Phys. J. A* **56**, 184 (2020), arXiv:2004.08136 [nucl-th].
- [80] Y. Kamiya, T. Hyodo, and A. Ohnishi, *Eur. Phys. J. A* **58**, 131 (2022), arXiv:2203.13814 [hep-ph].
- [81] Z.-W. Liu, J.-X. Lu, and L.-S. Geng, *Phys. Rev. D* **107**, 074019 (2023), arXiv:2302.01046 [hep-ph].
- [82] Z.-W. Liu, J.-X. Lu, M.-Z. Liu, and L.-S. Geng, *Phys. Rev. D* **108**, L031503 (2023), arXiv:2305.19048 [hep-ph].
- [83] I. Vidana, A. Feijoo, M. Albaladejo, J. Nieves, and E. Oset, *Phys. Lett. B* **846**, 138201 (2023), arXiv:2303.06079 [hep-ph].
- [84] N. Ikeno, G. Toledo, and E. Oset, *Phys. Lett. B* **847**, 138281 (2023), arXiv:2305.16431 [hep-ph].
- [85] M. Albaladejo, J. Nieves, and E. Ruiz-Arriola, *Phys. Rev. D* **108**, 014020 (2023), arXiv:2304.03107 [hep-ph].
- [86] J. M. Torres-Rincon, A. Ramos, and L. Tolos, *Phys. Rev. D* **108**, 096008 (2023), arXiv:2307.02102 [hep-ph].
- [87] M. Albaladejo, A. Feijoo, I. Vidaña, J. Nieves, and E. Oset, (2023), arXiv:2307.09873 [hep-ph].
- [88] A. Feijoo, L. R. Dai, L. M. Abreu, and E. Oset, *Phys. Rev. D* **109**, 016014 (2024), arXiv:2309.00444 [hep-ph].
- [89] K. P. Khemchandani, L. M. Abreu, A. Martinez Torres, and F. S. Navarra, *Phys. Rev. D* **110**, 036008 (2024), arXiv:2312.11811 [hep-ph].
- [90] H.-P. Li, J.-Y. Yi, C.-W. Xiao, D.-L. Yao, W.-H. Liang, and E. Oset, *Chin. Phys. C* **48**, 053107 (2024), arXiv:2401.14302 [hep-ph].

- [91] A. Feijoo, M. Korwieser, and L. Fabbietti, (2024), arXiv:2407.01128 [hep-ph].
- [92] J. A. Oller and E. Oset, Nucl. Phys. A **620**, 438 (1997), [Erratum: Nucl.Phys.A 652, 407–409 (1999)], arXiv:hep-ph/9702314.
- [93] S. E. Koonin, Phys. Lett. B **70**, 43 (1977).
- [94] S. Pratt, T. Csörgő, and J. Zimányi, Phys. Rev. C **42**, 2646 (1990).
- [95] W. Bauer, C. Gelbke, and S. Pratt, Annu. Rev. Nucl. Part. Sci. **42**, 77 (1992).
- [96] D. L. Mihaylov, V. Mantovani Sarti, O. W. Arnold, L. Fabbietti, B. Hohlweger, and A. M. Mathis, Eur. Phys. J. C **78**, 394 (2018).
- [97] Y. Kamiya, K. Sasaki, T. Fukui, T. Hyodo, K. Morita, K. Ogata, A. Ohnishi, and T. Hatsuda, Phys. Rev. C **105**, 014915 (2022).
- [98] J. Haidenbauer, Nucl. Phys. A **981**, 1 (2019).
- [99] S. Acharya *et al.* (ALICE Collaboration), Phys. Lett. B **811**, 135849 (2020), arXiv:2004.08018 [nucl-ex].
- [100] S. Acharya *et al.* (ALICE), (2023), arXiv:2311.14527 [hep-ph].
- [101] D. Mihaylov and J. González González, Eur. Phys. J. C **83**, 590 (2023), arXiv:2305.08441 [hep-ph].
- [102] A. Andronic, P. Braun-Munzinger, K. Redlich, and J. Stachel, Nature **561**, 321 (2018), arXiv:1710.09425 [nucl-th].
- [103] T. Pierog, I. Karpenko, J. M. Katzy, E. Yatsenko, and K. Werner, Phys. Rev. C **92**, 034906 (2015), arXiv:1306.0121 [hep-ph].
- [104] S. Navas *et al.* (Particle Data Group), Phys. Rev. D **110**, 030001 (2024).
- [105] X.-K. Dong, V. Baru, F.-K. Guo, C. Hanhart, and A. Nefediev, Phys. Rev. Lett. **126**, 132001 (2021), [Erratum: Phys.Rev.Lett. 127, 119901 (2021)], arXiv:2009.07795 [hep-ph].
- [106] M. Ablikim *et al.* (BESIII), Phys. Rev. Lett. **131**, 211902 (2023), arXiv:2308.15362 [hep-ex].
- [107] R. Lednický and V. L. Lyuboshits, Yad. Fiz. **35**, 1316 (1981).
- [108] A. Andronic, P. Braun-Munzinger, and J. Stachel, Nucl. Phys. A **772**, 167 (2006), arXiv:nucl-th/0511071.
- [109] A. Bazavov *et al.* (HotQCD), Phys. Rev. D **90**, 094503 (2014), arXiv:1407.6387 [hep-lat].
- [110] S. Borsanyi, Z. Fodor, C. Hoelbling, S. D. Katz, S. Krieg, and K. K. Szabo, Phys. Lett. B **730**, 99 (2014), arXiv:1309.5258 [hep-lat].

I. SUPPLEMENTAL MATERIAL

In this Supplemental Material, we provide further information that substantiates the results and conclusion obtained in the main text, including coupled-channel effects, input uncertainties, and the performance of the Lednický-Lyuboshits model.

A. Coupled-channel effects

In this section, in addition to the $D\bar{D}^*$ channel, we consider the relevant channel of $\pi J/\psi$, which plays an important role in the decay of $Z_c(3900)$. We refer to the $\pi J/\psi$ as channel 1 and $D\bar{D}^*$ as channel 2. The coupled-channel potential reads

$$V_{2\text{ch}}(\sqrt{s}) = \begin{pmatrix} 0 & c + d \frac{k_1^2 + k_2^2}{2} \\ c + d \frac{k_1^2 + k_2^2}{2} & a + b k_2^2 \end{pmatrix}, \quad (7)$$

where $k_i = \frac{\sqrt{s-(m_{i1}+m_{i2})^2}\sqrt{s-(m_{i1}-m_{i2})^2}}{2\sqrt{s}}$ represents the c.m. momentum of the i th channel, a , b , c , and d are real LECs to be determined. The $\pi J/\psi \rightarrow \pi J/\psi$ interaction is neglected due to the Okubo-Zweig-Iizuka suppression. Then, the coupled-channel T -matrix can be obtained as

$$T_{2\text{ch}}(\sqrt{s}) = [\mathbb{I} - V_{2\text{ch}}G_{2\text{ch}}]^{-1}V_{2\text{ch}}, \quad (8)$$

where $G_{2\text{ch}}$ is the diagonal matrix of loop functions. The generalized coupled-channel CF for a specific channel j reads [69, 83]

$$C_j(k_j) = 1 + \int_0^\infty d^3r S_{12} \left[\sum_i \omega_i \left| \delta_{ij} j_0(k_j r) + T_{ij} \tilde{G}_i \right|^2 - |j_0(k_j r)|^2 \right], \quad (9)$$

where ω_i is the weight for the individual components of the multi-channel wave function. Due to the lack of experimental information, we use the simplest statistic model [71, 108] to estimate the ratio of the weight ω_i/ω_j , which reads

$$\frac{\omega_i}{\omega_j} \approx \frac{\exp[-(m_{i1} - m_{i2})/T^*]}{\exp[-(m_{j1} - m_{j2})/T^*]}, \quad (10)$$

where the hadronization temperature is $T^* = 154$ MeV [109, 110]. The weight of the observed channel $\omega_{D^0 D^{*-}}$ is set at 1, and the calculated $\omega_{\pi^- J/\psi}$ equals 63.2 ($\omega_{K^- J/\psi}/\omega_{D^0 D_s^{*-}} \approx 12.3$ for $Z_{cs}(3985)$).

For the resonant state scenario, we utilize the mass and width of $Z_c(3900)$ suggested by the PDG [104]. Due to the introduction of new free parameters c and d , we further consider the experimental branching ratio $BR = \frac{\Gamma(Z_c(3885) \rightarrow D\bar{D}^*)}{\Gamma(Z_c(3900) \rightarrow \pi J/\psi)} = 6.2$ [36] ($\frac{\Gamma(Z_{cs}(3985)^+ \rightarrow K^+ J/\psi)}{\Gamma(Z_{cs}(3985)^+ \rightarrow (\bar{D}^0 D_s^{*+} + \bar{D}^{*0} D_s^+))} < 0.03$ [106]). Since the $D\bar{D}^*$ threshold is about 640 MeV above the $\pi J/\psi$ threshold, it is expected that the introduction of the $\pi J/\psi$

channel mainly affects the $Z_c(3900)$ width rather than its mass. Therefore, we first switch off the $\pi J/\psi$ channel and use the $Z_c(3900)$ mass and partial width ($\Gamma_{D\bar{D}^*} = \Gamma_{BR+1} \approx 24.5$ MeV) to fix the LECs a and b (similar to the single-channel study of the main text), and then use the mass and the full width ($\Gamma = 28.4$ MeV) to determine the remaining LECs c and d in the coupled-channel framework. For the virtual and bound state scenarios, only the constants a and c are retained in the potential, while b and d are set at 0. The corresponding poles are fine-tuned to obtain a line shape for the $D^0 D^{*-}$ IMS similar to the resonant state scenario. The pole settings, and the LECs a , b , c , and d are listed in Table I.

We present the coupled-channel $D^0 D^{*-}$ CFs for the three scenarios in Fig. 1. It is seen that the elastic parts of CFs are similar to the single-channel calculations, but full coupled-channel results are enhanced in all three scenarios. Especially in the resonant state scenario, the suppression in the high-momentum region is offset by the coupled-channel effect. This significant coupled-channel effect is mainly caused by the large $\omega_{\pi^- J/\psi}$. But considering the probability of binding $c\bar{c}$ should be less than that of binding $c\bar{q}$ or $\bar{c}q$, the realistic value of $\omega_{\pi^- J/\psi}$ may not be so large. In any case, one can still distinguish the three scenarios by measuring the significant difference in the low-momentum $D^0 D^{*-}$ CFs.

B. Effect of the uncertainty of pole positions

To check the effect of pole positions on the correlation functions, we adopt the uncertainties of the latest PDG averages for the resonant state and obtain the corresponding uncertainties for the virtual and bound states demanding similar line shapes of the invariant mass spectrum, e.g., $Z_c(3900)$: resonant state $M = 3887.1 \pm 2.6$ MeV and $\Gamma = 28.4 \pm 2.6$ MeV [104], virtual state $M = 3871_{-0.7}^{+0.5}$ MeV, bound state $M = 3867_{-1.2}^{+1.8}$ MeV; $Z_{cs}(3985)$: resonant state $M = 3988 \pm 5$ MeV and $\Gamma = 14 \pm 4$ MeV [104], virtual state $M = 3974_{-1.0}^{+1.3}$ MeV, bound state $M = 3972_{-2.2}^{+2.5}$ MeV.

We show the pole-position dependence of the $D^0 D^{*-}$ and $D^0 D_s^{*-}$ CFs in Figs. 2 and 3, respectively. For the resonant state scenario (especially for $Z_{cs}(3985)$), the peaks and minima near the resonant energy gradually evolve into low-momentum enhancement and high-momentum suppression as $\Gamma/2$ increases. This structure gradually shifts towards the high-momentum region and diminishes as $\Delta M = M - m_1 - m_2$ increases. For the virtual state scenario, the CFs are always greater than unity and decrease as the virtual-state pole moves away from the threshold. For the deep bound state scenario, the CFs are always smaller than unity, and this suppression becomes more obvious with increasing binding energy. It is worth noting that in the bound state scenario of $Z_{cs}(3985)$, the CF at $\Delta M = -2.5$ MeV exhibits the feature of a shallow bound state, namely, the low-momentum result is above unity for small R . These general features for the bound state scenario have been demonstrated based on the square-well model in our previous work [81]. In summary, it is seen that even accounting for the uncertainties of pole positions, the femtoscopic CFs can still distinguish whether $Z_c(3900)$

TABLE I. Masses and widths of $Z_c(3900)$, and the LECs a , b , c , and d in the coupled-channel framework. The sharp cutoff q_{\max} is fixed at 1 GeV.

Scenario	M [MeV]	Γ [MeV]	a	b [$10^{-6} \cdot \text{MeV}^{-2}$]	c	d [$10^{-6} \cdot \text{MeV}^{-2}$]
$Z_c(3900)$	resonant	3887.1 [104]	28.4 [104]	-99.0	-1594.2	-123.6
	virtual	3871.7	2.0	-138.9	0	-19.4
	bound	3868.4	0.9	-192.0	0	-13.2

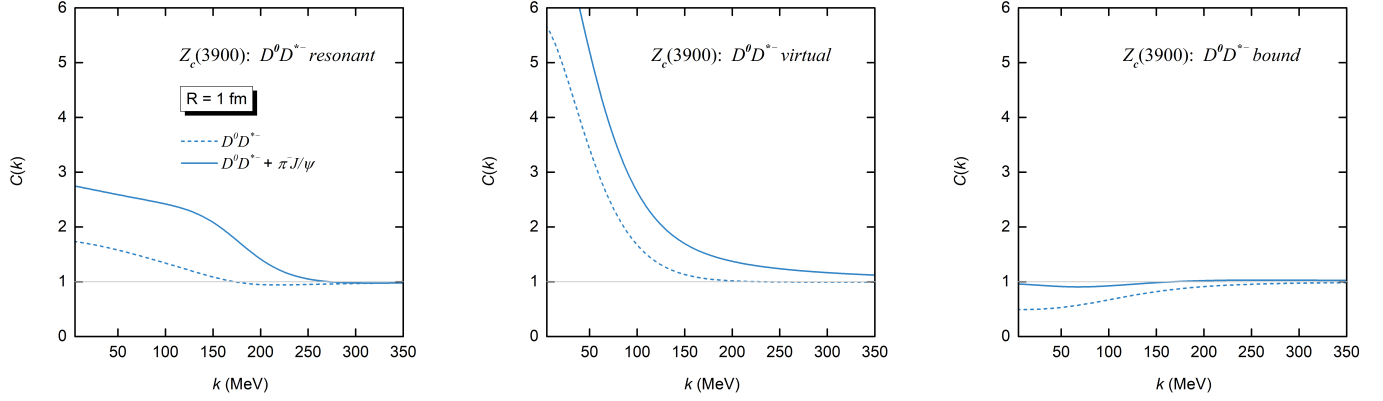


FIG. 1. Coupled-channel $D^0 D^{*-}$ correlation functions for $R = 1$ fm as a function of the relative momentum k . The dashed and solid lines denote the elastic contribution and full coupled-channel result, respectively. The sharp cutoff q_{\max} is fixed at 1 GeV.

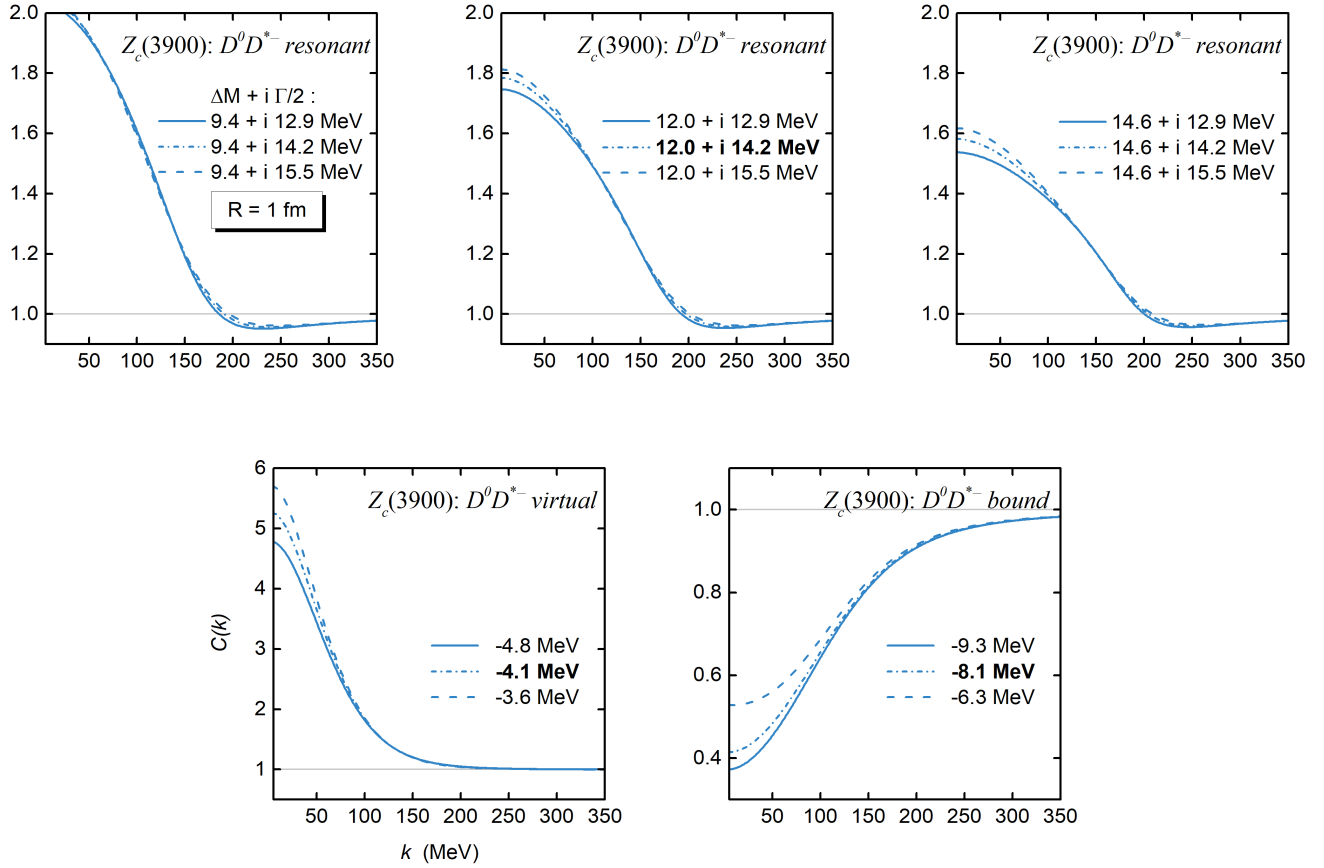


FIG. 2. Pole-position dependence of the $D^0 D^{*-}$ correlation functions. The source size is set at $R = 1$ fm, and the hard cutoff q_{\max} is fixed at 1 GeV.

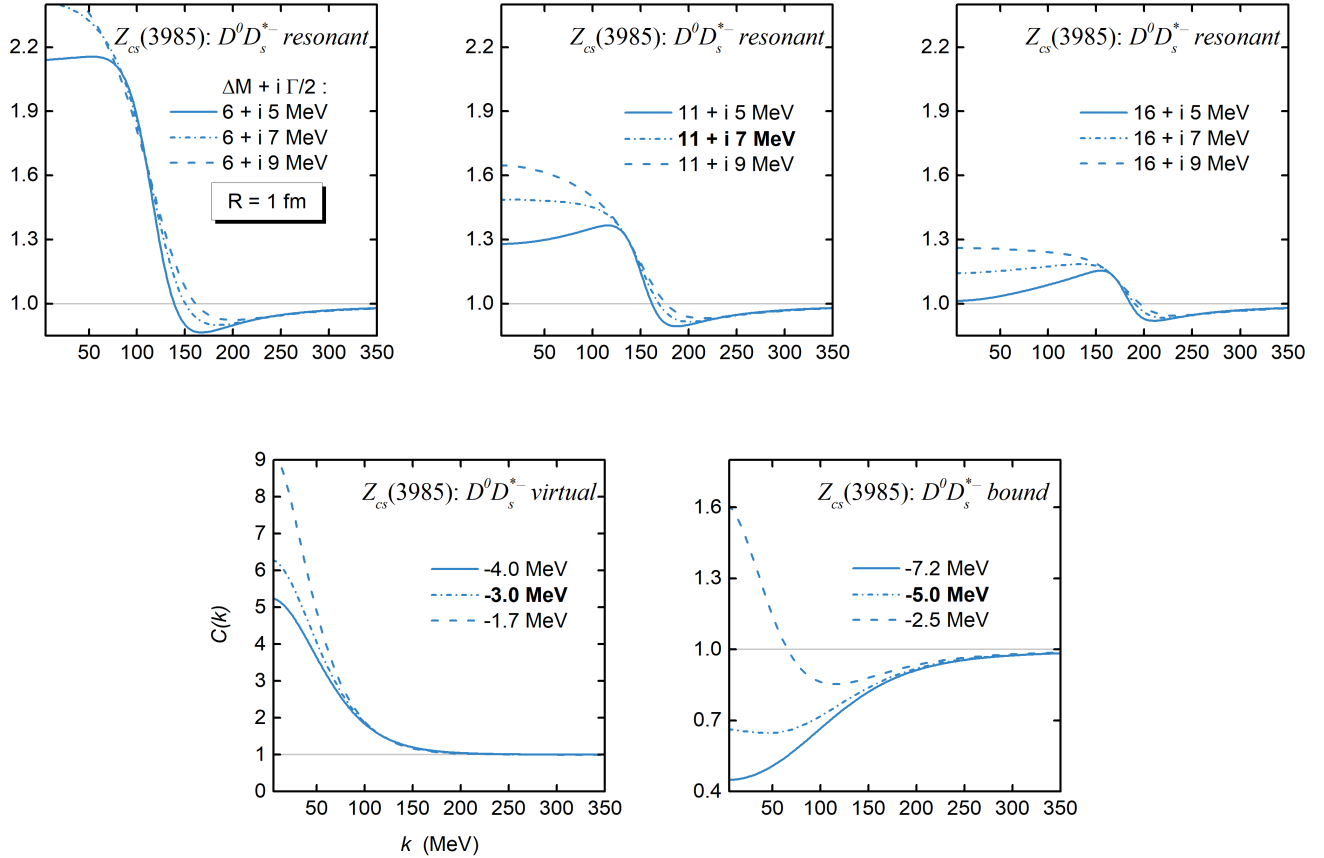


FIG. 3. Pole-position dependence of the $D^0 D_s^{*-}$ correlation functions. The source size is set at $R = 1$ fm, and the hard cutoff q_{\max} is fixed at 1 GeV.

and $Z_{cs}(3985)$ are resonance, virtual, or bound states.

C. General features of CFs and comparison with the Lednický-Lyuboshits model

In the following, we review the Lednický-Lyuboshits (LL) model [107], which has been widely used in the experimental and theoretical studies of CFs [37, 38]. For systems with two non-identical particles and without Coulomb interaction, the CF can be expressed as

$$C(k) = 1 + \int_0^\infty d^3r S_{12} \left[|\psi|^2 - |j_0|^2 \right], \quad (11)$$

where ψ is the S -channel wave function. Assuming a Gaussian source $S_{12} = \exp[-r^2/(4R^2)]/(2\sqrt{\pi}R)^3$ and replacing ψ everywhere with the asymptotic form

$$\psi(r) \approx \psi_{\text{asy}}(r) = e^{-2i\delta} \left[\frac{\sin kr}{kr} + f \frac{e^{ikr}}{r} \right], \quad (12)$$

where δ is the phase shift and f is the scattering amplitude, the CF becomes

$$C_{\text{LL-I}}(k) = 1 + \frac{|f|^2}{2R^2} + \frac{2\text{Re}f}{\sqrt{\pi}R} F_1 - \frac{\text{Im}f}{R} F_2, \quad (13)$$

where $F_1 = \int_0^x dt \exp(t^2 - x^2)/x$, $F_2 = [1 - \exp(-x^2)]/x$, and $x = 2kR$. Here, f is given by the effective range expansion (ERE) $f \approx (-1/a_0 + r_{\text{eff}}k^2/2 - ik)^{-1}$. In the low-momentum region, the deviation from the asymptotic wave function can be evaluated by using the effective range formula [68]

$$\lim_{k \rightarrow 0} \frac{1}{|f|^2} \int_0^\infty r^2 dr \left[|\psi|^2 - |\psi_{\text{asy}}|^2 \right] = -\frac{1}{2} r_{\text{eff}}. \quad (14)$$

When we insert a factor $\exp[-r^2/(4R^2)]$ within the integral of Eq. (14), the resulting integral can serve as the correction for Eq. (13). This factor is expected to have an insignificant impact on the integral result as long as R is large compared with the interaction range. Based on this assumption, we arrive at the CF in the so-called LL model

$$\begin{aligned} C_{\text{LL-II}}(k) &= 1 + \frac{|f|^2}{2R^2} + \frac{2\text{Re}f}{\sqrt{\pi}R} F_1 - \frac{\text{Im}f}{R} F_2 \\ &\quad - \frac{|f|^2}{4\sqrt{\pi}R^3} r_{\text{eff}}, \end{aligned} \quad (15)$$

where the last term represents the effective range correction. Generally, the ERE is valid near the threshold. Away from the threshold, the ERE may break down. For instance, with $a_0 = 0.18$ fm and $r_{\text{eff}} = -17.77$ fm, the scattering amplitude predicts a bound state pole below the threshold. However, this finding contradicts the resonant state pole of $\Delta M + i\Gamma/2 = 10 + i1$ MeV that was introduced initially. To avoid this problem, we adopt an alternative representation of

the scattering amplitude $f = (k \cot \delta - ik)^{-1}$. Then, Eq. (13) can be rewritten in the following form

$$\begin{aligned} C_{\text{LL-III}}(k) &= 1 + \left[\exp(-x^2) + \frac{2xF_1}{\sqrt{\pi}} \cot \delta \right] \frac{2}{x^2} \\ &\quad \times \frac{1}{1 + \cot^2 \delta}, \end{aligned} \quad (16)$$

where we resort to the non-relativistic Breit-Wigner shape for $\cot \delta = -k_R/k \cdot (k^2 - k_R^2)/(2\mu) \cdot 2/\Gamma$ to capture the general features of f at the resonant energy [85], where μ is the reduced mass of the hadron pair, k_R is the resonant momentum corresponding to the resonance mass. In the following analyses, we refer to Eqs. (13), (15), and (16) as the LL-I, LL-II, and LL-III models, respectively.

Without losing generality and focusing on the charm sector, the masses of the two particles m_1 and m_2 are chosen as 1.8 and 2 GeV, close to the masses of D and \bar{D}^* . For the resonant state case, the real part of the pole position with respect to the threshold $\Delta M = M - m_1 - m_2$ is set at 2.5, 5, and 10 MeV, respectively; the imaginary part of the pole position (half-width) $\Gamma/2$ is set at 1 and 10 MeV, respectively. For the virtual and bound state cases, ΔM is set at -2.5, -5, and -10 MeV, respectively. The parameters a and b are required to generate the above poles, and the corresponding scattering parameters are shown in Table II.

The corresponding CFs are displayed in Fig. 4. For a resonant state with a narrow width ((a-1)-(a-3) panels), the CF exhibits a peak at momentum slightly below k_R and a valley at momentum slightly above k_R . However, the peak evolves into an overall enhancement in the low-momentum region for a resonant state with a larger width ((b-1)-(b-3)). In contrast, the valley in the high-momentum region becomes less pronounced. In addition, the enhancement and suppression weaken as k_R moves toward the high-momentum region. For the virtual state case ((c-1)-(c-3)), the CFs are always greater than unity for various source sizes, indicating the existence of a purely attractive interaction. Meanwhile, the attractive strength decreases as the virtual-state pole moves away from the threshold, reducing the CF. This behavior is consistent with the variation of the parameter a and the scattering length with the pole position. For the deep bound state case ((d-2)-(d-3)), the CFs are always smaller than unity, and this suppression becomes more obvious with increasing binding energy. For the shallow bound state case (d-1), the low-momentum result is above unity for small R while below unity for large R .

Next, we compare the exact CFs and LL model results for $R = 1$ fm, where the scattering parameters and the resonant pole positions listed in Table II are employed in the LL-I/LL-II and LL-III models, respectively. For the virtual and bound state cases (see panels (c-1)-(c-3) and (d-1)-(d-3)), the exact CFs can be reproduced by the LL-II model, which is attributed to the sufficiently small effective ranges r_{eff} compared to the source size. However, for the resonant state case, the values of r_{eff} are significantly larger than the source size, which means that the effective range correction may not be appropriate. Thus, we compare the exact CFs with the LL-I results for the broad resonant state case. As shown in panels (b-1)-(b-3),

TABLE II. Resonant, virtual, and bound state pole positions with respect to the $m_1 + m_2$ threshold, the values of the parameters a and b , and the scattering length a_0 and effective range r_{eff} . The sharp cutoff q_{max} is fixed at 1 GeV.

	$\Delta M + i \Gamma/2$ [MeV]	a	b [$10^{-6} \cdot \text{MeV}^{-2}$]	a_0 [fm]	r_{eff} [fm]
resonant	2.5 + i 1	-108.20	-9234.37	-0.72	-29.43
	5 + i 1	-29.21	-12934.30	-0.07	-570.77
	10 + i 1	195.34	-18219.00	0.18	-17.77
	2.5 + i 10	-127.67	-1260.96	-1.43	-2.62
	5 + i 10	-121.38	-1439.80	-1.12	-3.39
	10 + i 10	-102.39	-1796.48	-0.61	-6.16
virtual	-2.5	-139.94	0	-2.73	0.29
	-5	-133.68	0	-1.89	0.29
	-10	-125.38	0	-1.30	0.29
bound	-2.5	-175.32	0	3.01	0.28
	-5	-183.81	0	2.18	0.28
	-10	-196.56	0	1.59	0.28

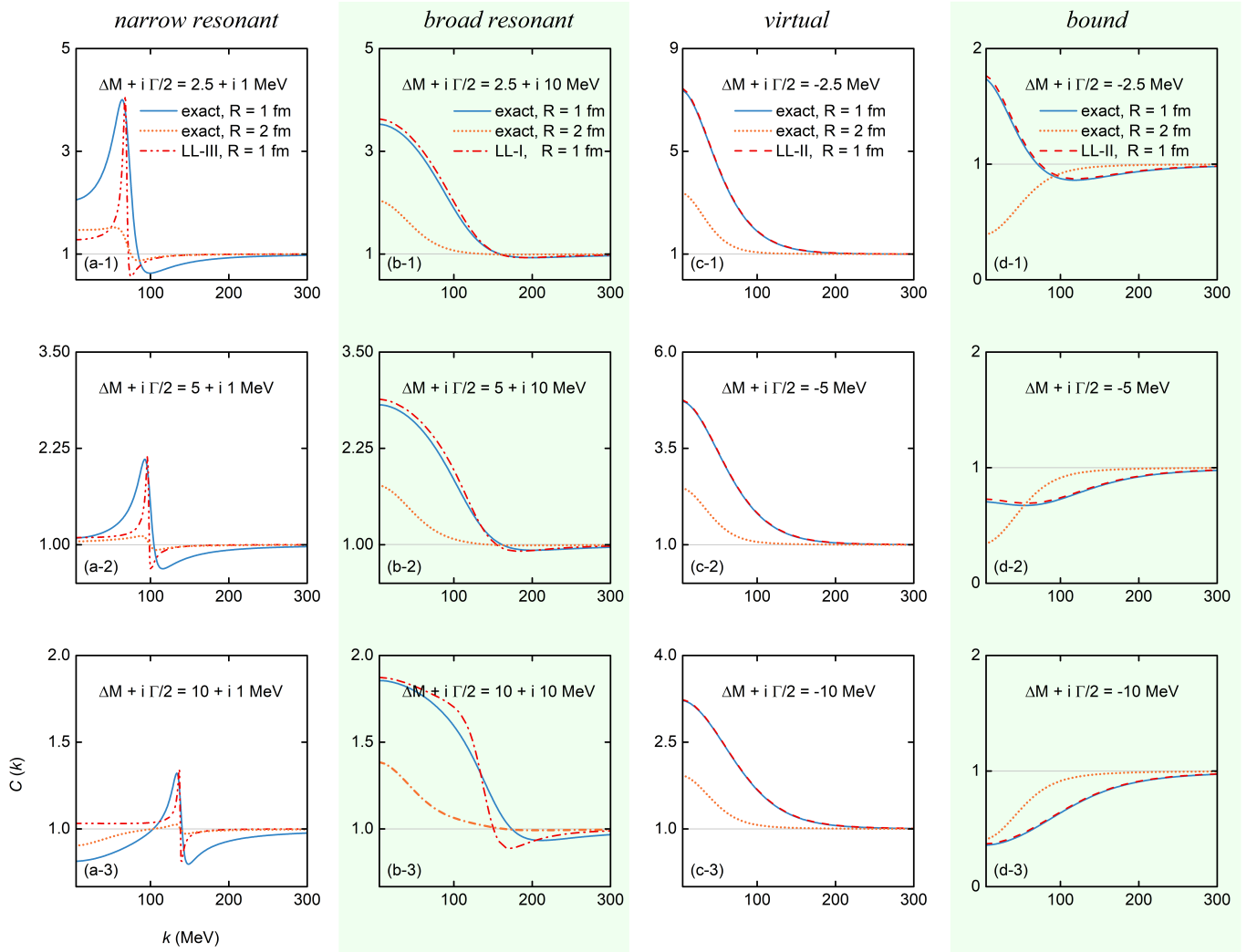


FIG. 4. Correlation functions corresponding to potentials capable of generating a resonance (a and b panels), virtual state (c panels), or bound state (d panels) with the pole position $\Delta M + i \Gamma/2$ specified in the respective plots. The source size is set at $R = 1$ and 2 fm, and the hard cutoff q_{max} is fixed at 1 GeV. The results obtained with the LL-I, LL-II, and LL-III models are shown as red dash-dotted, dashed, and dash-dot-dotted lines for comparison, respectively. For more details, see the main text.

the LL-I model can approximate the exact CFs. However, as the resonance moves away from the threshold, the ERE gradually breaks down, and the difference between the LL-I results and the exact CFs increases. For the narrow resonant state case (see panels (a-1)-(a-3)), since the ERE has lost the feature of a resonant state, we have to compare the exact CFs with the LL-III results. It is seen that the LL-III results may deviate from the exact results at zero momentum, but they behave similarly to the exact CFs near the resonant energy.

In addition, we also compare the exact $D^0 D^{*-}$ and $D^0 D_s^{*-}$ CFs with the results from the LL model. Similarly, the LL-II model can reproduce the CFs for virtual and bound states. However, for the resonant state scenarios where $|r_{\text{eff}}|$ is much larger than the source size, the LL-II model breaks down due to substantial deviations introduced by the effective range correction. Meanwhile, the LL-I model performs well in reproducing CFs in the low-momentum region, whereas the LL-III model can reproduce results in the high-momentum region.